

© 2016

Xiaobing Zhang

ALL RIGHTS RESERVED

**NUMERICAL SIMULATION AND EXPERIMENTAL REALIZATION OF A
THERMOSYPHON BASED HYBRID SOLAR THERMOELECTRIC POWER
GENERATOR**

By

XIAOBING ZHANG

A thesis submitted to the

Graduate School-New Brunswick

Rutgers, the State University of New Jersey

In partial fulfillment of the requirements

For the degree of

Master of Science

Graduate Program in Mechanical and Aerospace Engineering

Written under the direction of

Mona Zebarjadi & Yogesh Jaluria

And approved by

New Brunswick, New Jersey

October, 2016

ABSTRACT OF THE THESIS

Numerical simulation and experimental realization of a thermosiphon based
hybrid solar thermoelectric power generator

by XIAOBING ZHANG

Thesis Director:

Mona Zebarjadi

Thermosyphons are highly efficient systems for converting sunlight into heat and transferring heat to provide hot water. Thermoelectric (TE) power generators are proposed recently as a topping cycle incorporated in series with thermosyphons. In this work, we propose a new design, which places TE power generators thermally in parallel with thermosiphon-based solar water-heating systems. The solar heat is radiated on the collector (evaporator) zone and transferred through the copper pipe into two parallel channels: a phase-change liquid that acts as the heat transfer medium for the water heating set-up and the thermoelectric module used to generate electricity. We performed both numerical simulation and experimental realization of the proposed setup. Experimental validation of the model from a home-made prototype and parallel system optimization are completed. This study opens up a promising possibility to efficiently convert solar energy to useful thermal and electrical energy.

Nomenclature

A	Area (m^2)
C_p	Specific heat capacity (J/kg K)
E	Energy (J)
G	Gravitational acceleration (m/s^2)
G	Incident radiative heat flux (W/m^2)
H	heat transfer coefficient ($\text{W/m}^2\text{K}$)
h_p	Enthalpy of phase p
κ	Thermal conductivity (W/mK)
K	Thermal conductance (W/K)
L	Length (m)
\dot{m}	Mass flux ($\text{kg/m}^2 \text{ s}$)
Nu	Nusselt number
P	Pressure (Pa)
P_E	Power generated (W)
Pr	Prantl number
Q	Heat transfer from heat pipe to top (W)
Q_{conv}	Convection heat transfer (W)
Q_{rad}	Radiation heat transfer (W)
R	Reflectivity; Electrical resistance
Re	Reynolds number
S	Seebeck coefficient

I	Incoming solar radiation (W/m ²)
I_t	Transmitted solar radiation (W/m ²)
I_r	Reflected solar radiation (W/m ²)
t_{TE}	TE leg thickness (m)
r_{pipe}	Pipe outer radius (m)
T	Temperature (K)
T_{SS}	Selective surface (Evaporator) temperature (K)
T_{cond}	Condenser temperature (K)
T_{glass}	Glass temperature (K)
T_m	Average temperature of thermoelectric leg
V	Velocity (m/s)
V_f	Volume Fraction
Z	Figure of merit

Greek symbols

α	Absorptivity;
γ	$\sqrt{1 + ZT_m}$
ε	Emissivity
η	Efficiency
ζ	Electrical resistivity ($\Omega \cdot m$)
ρ	Density (kg/m ³)
σ_0	Stefan-Boltzmann constant (W/m ² K ⁴)

σ Surface tension (N/m)

τ Transmissivity

Abbreviation

CFD Computational fluid dynamics

TE TE

UDF Users' defined function

VOF Volume of fluid

PV Photovoltaic

Subscripts

h, c Hot, cold

p, n p, n legs

W Wall

S_s Selective surface

l,g Liquid, gas phases

Content

ABSTRACT OF THE THESIS	ii
Nomenclature	iii
Chapter 1 Introduction	1
1.1 Solar Water Heaters	1
1.2 Thermosyphons & TE modules.....	2
1.3 Thermosyphon-based Hybrid Solar Water Heaters	3
Chapter 2 Numerical Modelling	5
2.1 Solar Radiation Absorption.....	5
2.2 TE module Modelling	11
2.3 Governing Equations for Modelling the Thermosyphon	12
2.4 Boundary Conditions & Initialization	14
Chapter 3 Experiments.....	16
3.1 Experimental Design	16
3.2 System Description	17
3.2.1 TE Module.....	17
3.2.2 Heater.....	18
3.2.3 Heat Pipe.....	19
3.2.4 Water Cooling Channel	20

3.2.5 Thermocouples	20
3.2.6 System Insulation	21
3.2.7 Accessories	21
Chapter 4 Results & Discussion	22
4.1 Comparison of Experiments and Simulation	22
4.2 Parallel System Optimization.....	23
4.2.1 Effect of Thickness of TE.....	24
4.2.2 Effect of Length of TE.....	25
4.2.3 Effect of Pipe Radius	26
Chapter 5 Conclusion.....	28
References	29

Chapter 1 Introduction

1.1 Solar Water Heaters

Green energy is urgently needed due to global warming and harmful pollution from fossil fuels. The abundance of solar power provides one possibility to meet our increasing need for clean energy. There have been many technologies developed to capture solar energy and convert it to other useful forms of energy. While solar photovoltaics (PV) convert sunlight directly to electricity, solar thermal processes convert solar energy to thermal energy. The generated thermal energy could be either used directly or converted into mechanical and electrical energies. Examples of direct use of thermal energy include: passive space heating, solar cookers, solar driers, and solar water heaters [1]. Examples of technologies to convert solar thermal energy to electrical energy include: concentrated solar power (CSP), solar TEs (STE) and solar chimney [2]. While CSPs are large-scale systems, TE modules can be used as small power generators for example in buildings and car engines. In this work, we focus on small-scale residential applications.

Residential solar water systems are popular in many countries such as China, Germany, and Italy [3]. Solar water heater systems are often based on heat-pipes or thermosyphons for efficient heat transfer with minimal heat loss. Two-phase thermosyphons demonstrate a simple, but effective way of collecting and transferring solar energy using the large latent heat of the enclosed phase change liquid [4]. The working principle is as follows: solar heat is collected at the outer surface of the evaporator. The collected heat is transferred to the enclosed liquid. As a result, the liquid absorbs a substantial amount of heat owing to its large liquid-gas latent heat and evaporates. By natural convection, the produced lighter vapour rises

up to the condenser where it condenses back into liquid. The liquid is returned to the evaporator by gravity. A thermosyphon can achieve very high effective thermal conductivity, as a result of a fast and large heat transfer rate through the phase-change process.

1.2 Thermosyphons & TE modules

Thermosyphons have been investigated and modelled extensively in the past. For example, Alizadehdakhel [5] presented CFD modelling of the evaporation and condensation effects in a two-phase thermosyphon and achieved good agreement with experimental data collected. Fadhl [6] performed similar numerical modelling for a two-phase closed thermosyphon and obtained a temperature distribution that agreed with the experimental results.

Recently, hybrid systems are proposed for the purpose of cogeneration of residential heat (hot water) and electricity [7]. These new hybrid systems combine either solar PVs or STEs with solar hot water systems [8-10]. Miljkovic et al. [8] proposed to concentrate solar heat on small TE modules to produce electricity and use a thermosyphon to transfer the waste heat. In another design, He et al. [12] proposed a solar heat pipe-TE generator unit, in which TE modules serve as a bridge between the condenser zone and the cooling water flux. In all of these designs, TE modules are placed thermally in series with the thermosyphons and thermal or optical concentration is used to focus a large heat flux on the thermoelectric modules.

Contrary to thermosyphons, TE modules have very small thermal conductivities and large thermal resistances, enabling establishment of large temperature differences over their small length. In a recent article, it was shown that imposing large heat fluxes on one side of TE modules, without extensive cooling of the other side, resulted in over heating of the TE legs and therefore a lowering of the performance [13]. Similarly, TE modules in series arrangement, serve as a thermal bottleneck and result in over heating of the heat pipe. As a

result, He et al. [10] reported an in-series hybrid efficiency that was well below the efficiency of the thermosyphon alone. While for our parallel design, there is no such shortcoming.

1.3 Thermosyphon-based Hybrid Solar Water Heaters

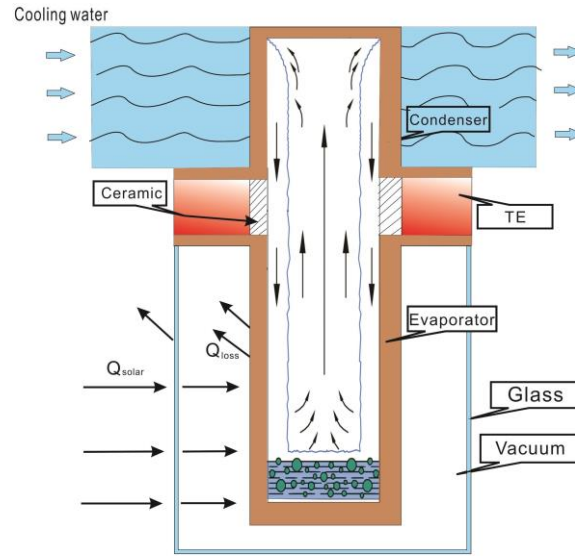


Fig. 1. Schematic drawing of hybrid thermoelectric-solar water heater designs

In this work, we propose to add TE modules in parallel to the thermosyphon heat flux as shown in Fig. 1. The Condenser and evaporator zones are separated by the TE module. The heat pipe functions normally, allowing the heat transfer fluid to evaporate and condense uninterrupted. The pipe is cut near the condenser bulb, and the TE replaces a section of copper piping. The temperature difference across the evaporator and the condenser manifests as a similar temperature gradient across the TE legs. This temperature drop is used to generate electricity. In this design, TE modules do not block the large heat flux. Instead the design is able to effectively heat water as if there were no TE, but utilizes an inherent temperature difference to generate power. This uses more of the absorbed solar power, and is the reason behind the increased hybrid efficiency. The heat pipe is coated with a selective surface absorber layer to maximize absorption of the visible and near field infrared solar radiation

while reducing irradiation losses at the far-field infrared range. A thermally evacuated twin chamber is used to minimize the convective and radiative heat losses.

Chapter 2 Numerical Modelling

The thermosyphon is numerically modelled with CFD simulation using ANSYS FLUENT 14.5 [14] to simulate the liquid-gas phase change of the working fluid and conduction inside the pipe and thermoelectric module, while an energy balance is used to simulate the glass cover and selective surfaces. The convection model has been validated by comparing it with benchmark results [15]. And a residual less than 10^{-4} is used for the convergence test. Finally, the accuracy of thermosyphon modelling using ANSYS FLUENT has been validated by Ali and Kafeel [5, 17] and therefore we adapt the same model for the part of the simulation that deals with the heat pipe. Finally the numerical results are compared with experimentally measured values to validate the approach. The comparison will be discussed in section 4.1.

2.1 Solar Radiation Absorption

We use the solar spectral irradiance for Air Mass of 1.5. [18] A low-iron glass (0.318 cm thick)

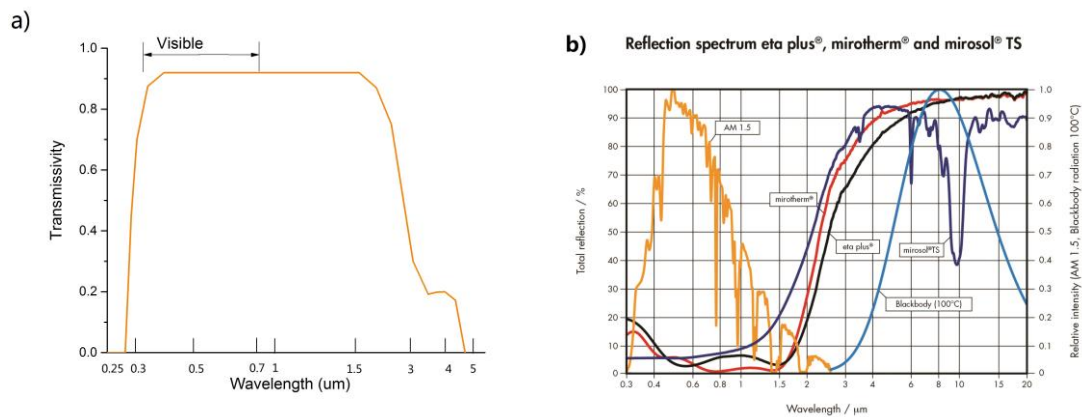


Fig. 2. Transmissivity of the chosen glass and reflectivity of the chosen selective surface. Copyrighted by: a) McGraw-Hill Education; b) © ALANOD GmbH & Co. KG.

is used to minimize the convective and radiative heat losses. Selective surface Mirotherm® is

modeled onto the evaporator to enhance solar absorption. The transmissivity of the chosen glass $\tau_g(\lambda)$ [19] and the reflectivity of the chosen selective surface $R_{ss}(\lambda)$ [20] are shown in Fig. 2.

Solar radiation absorbed by the selective surface could be written as: [19]

$$I_{absorbed} = \int_0^{\infty} \tau_g(\lambda) \alpha_{ss}(\lambda) I_o(\lambda) d\lambda \quad (1)$$

Eq. (1) integrates over the whole solar wavelength spectrum [18] to calculate the total solar radiation absorbed by the selective surface. $I_o(\lambda)$ is the solar spectrum irradiance (for AM1.5). This solar spectrum along with the solar spectrum after passing through the glass ($\tau_g(\lambda)I_o(\lambda)$) and the spectrum absorbed by the selective surface ($\tau_g(\lambda)\alpha_{ss}(\lambda)I_o(\lambda)$) are shown in Fig. 3. Assuming zero transmissivity for the selective surface, the emissivity, absorptivity and reflectivity are related by:

$$\alpha_{ss}(\lambda) = \varepsilon_{ss}(\lambda) = 1 - R_{ss}(\lambda) \quad (2)$$

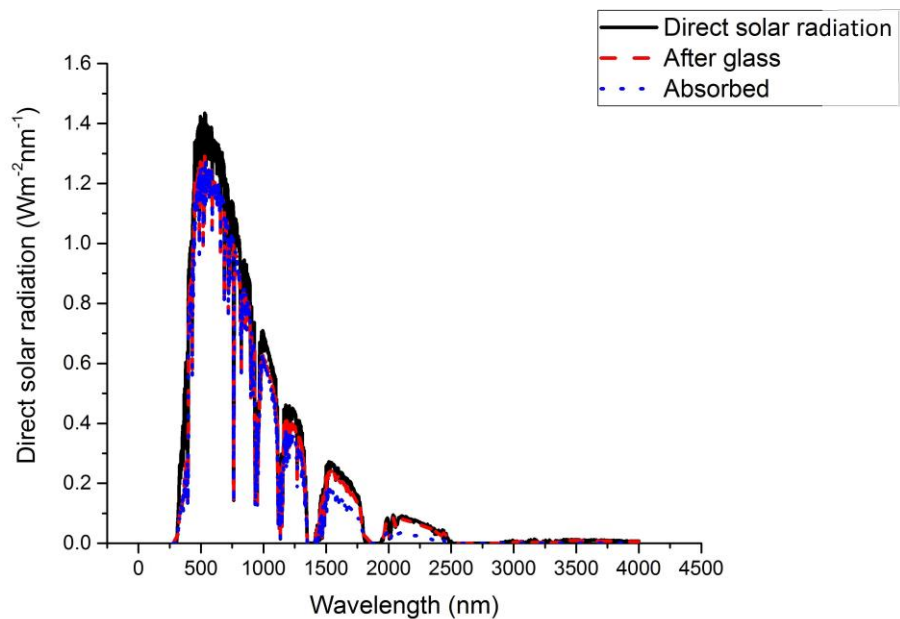


Fig. 3. Black solid line: Solar spectrum of AM1.5, Red dashed line: solar spectrum after passing through the glass layer and Blue dotted line: spectrum absorbed by the selective surface.

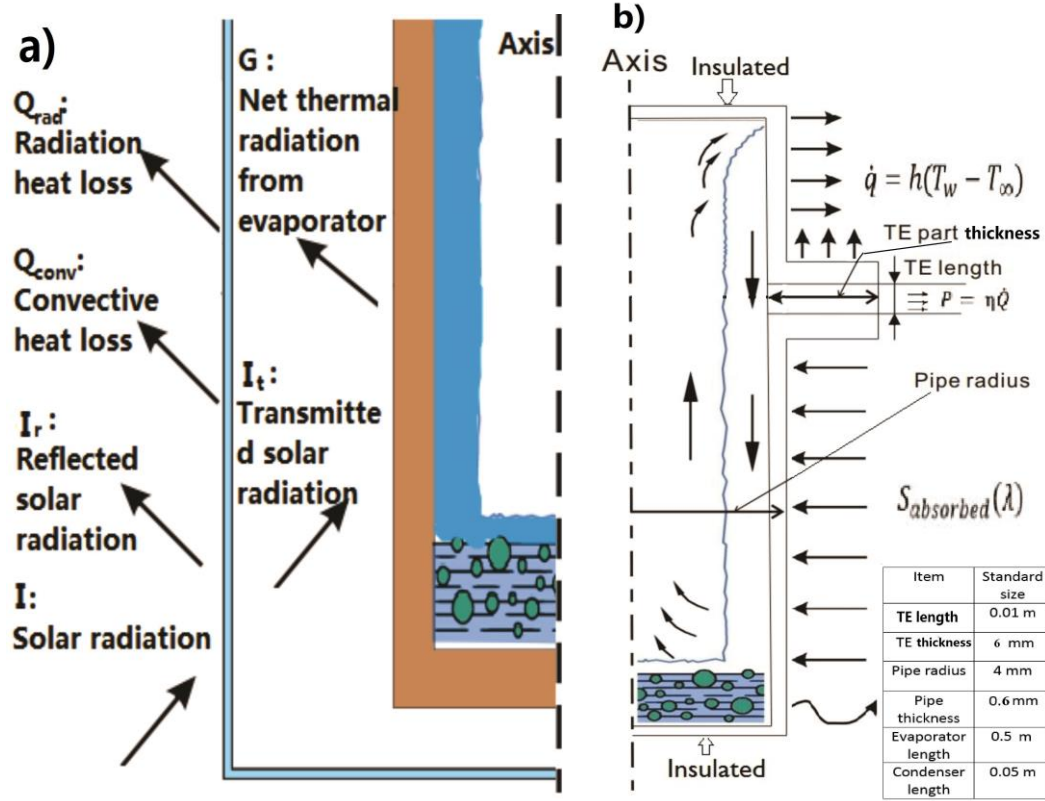


Fig. 4. a) Energy balance of the glass layer. b) Boundary conditions of the system.

At steady state condition, the incoming energy equals to the outgoing energy. This is schematically shown in Fig. 4a. The energy balance for the glass is therefore [21]:

$$I + G = I_t + I_r + Q_{conv} + Q_{rad} \quad (3)$$

Here, the incoming energies are solar radiation (I) and net thermal irradiation from evaporator (G). Assuming the net thermal irradiation energy is fully absorbed/reflected by the glass, the outgoing energy terms are: reflected solar radiation (I_r), convection and radiation heat loss from the glass to the environment (Q_{conv} and Q_{rad} respectively) and transmitted solar radiation (I_t). The assumption of zero transmissivity for G (infrared range)

is justified considering the transmissivity profile shown in Fig. 2a. The absorbed solar radiation by glass is $I_\alpha = I - I_r - I_t$. Therefore, we can rewrite Eq. 3 as:

$$I_\alpha + G = Q_{conv} + Q_{rad} \quad (4)$$

Since we assumed the glass is opaque to thermal radiation, the net irradiation heat transfer from the evaporator to the glass considering geometrical view factors for cylindrical shape is [19]:

$$G = \frac{\sigma_0(T_{ss}^4 - T_{glass}^4)}{\frac{1 - \varepsilon_{ss}}{A_{ss}\varepsilon_{ss}} + \frac{1}{A_{ss}F_{ss-glass}} + \frac{1 - \varepsilon_{glass}}{A_{glass}\varepsilon_{glass}}} \quad (5)$$

Which takes into account, multiple reflections in between the evaporator and the glass cylinders. $(1 - \varepsilon_{ss})/(A_{ss}\varepsilon_{ss})$, $1/(A_{ss}F_{ss-glass})$ and $(1 - \varepsilon_{glass})/(A_{glass}\varepsilon_{glass})$ are the evaporator, the separation space between evaporator/glass and the glass thermal resistance, respectively. $F_{ss-glass}$ is the view factor between selective surface and glass plate. Wavelength dependence of emissivity is considered before solving the energy balance equation. Inserting Eq. 5 into Eq. 4, the energy balance equation for the glass can be rewritten as:

$$\alpha_{glass}I_0A_{glass} + \frac{\sigma_0(T_{ss}^4 - T_{glass}^4)}{\frac{1 - \varepsilon_{ss}}{A_{ss}\varepsilon_{ss}} + \frac{1}{A_{ss}F_{ss-glass}} + \frac{1 - \varepsilon_{glass}}{A_{glass}\varepsilon_{glass}}} = hA_{glass}(T_{glass} - T_\infty) + \varepsilon_{glass}\sigma_0A_{glass}(T_{glass}^4 - T_\infty^4) \quad (6)$$

Assuming zero thermal resistance between the selective surface and the copper pipe, the temperature of the selective surfaces T_{ss} is the same as the temperature of the outer surface

of the evaporator T_{eva} . Since the solar intensity, materials properties and geometries are given, from Eq. 6, we can calculate T_{glass} as a function of T_{ss} using Bisection method and tabulating the results as shown in table. 1. Note that in the table 1 and simulations presented here, the ratio of A_{ss}/A_{glass} is fixed to 0.8. Figure 4b shows the default dimensions chosen in this simulation. These dimensions are chosen after commercial thermosyphon and TE modules.

Table 1 Relationship between T_{glass} and T_{ss} .

T_{ss}/K	T_{glass}/K	G/W
370	307.1661	0.548
380	307.6019	0.651
390	308.0719	0.787
400	308.5785	0.892
410	309.1229	1.031
420	309.7076	1.225
430	310.3326	1.473
440	311.0004	1.786
450	311.7133	2.083
475	313.7006	2.48
500	316.0004	2.93

The total heat loss G out from the evaporator is also just a function of T_{ss} for the given geometry and is shown in table 1. This heat loss can be implemented in the simulation by

Users' Defined Function (UDF) in FLUENT [22]. In this thesis, most results are calculated without the implementation of UDF. For those cases without UDF, radiation heat transfer coefficient is set to be 0.75 W/m²K. But at some points in Fig. 12 (a), the results with UDF and the results without UDF are simulated and compared accordingly.

2.2 TE module Modelling

The best TE material known for room temperature applications is bismuth antimony telluride and therefore we choose the materials properties given by [23] for p-type BiSbTe and [24] for n-type. Since the thermal conductivity of n & p legs are similar, we include the TE module as BiTe material with thermal conductivity of 1.5 W/m-K [23]. To do so, we use constant materials properties model. In this standard model [25] the energy conversion efficiency of a thermoelectric module could be written as:

$$\eta = \frac{I[S\Delta T - IR]}{K\Delta T + SIT_h - \frac{1}{2}I^2R} \quad (7)$$

K and R are the total thermal conductance and electrical resistance, and S is the Seebeck coefficient of the thermoelectric module. The maximum efficiency occurs when the external load (R_L) is matched to the internal resistance by a factor of $\gamma = \sqrt{1 + ZT_m}$.

$$R_L = R\gamma = R\sqrt{1 + \frac{S^2(T_h + T_c)}{2KR}} \quad (8)$$

As a result, the optimum efficiency of the TE module (optimized versus current and geometry) is expressed as a function of hot and cold end temperature and material figure of merit (ZT_m):

$$\eta_{opt} = \frac{(\gamma-1)\Delta T}{[(\gamma+1)T_h - \Delta T]} \quad (9)$$

Given the materials properties, efficiency is only a function of temperatures on the sides and could be used to subtract the generated power P_E from the net heat flux entering the hot side \dot{Q} ,

$$P_E = \eta_{opt} \dot{Q} \quad (10)$$

After the simulation is finished, the optimum efficiency of the TE module can be calculated based on Eq. (9). And the net heat flux transferred through the TE module is computed directly from the program. So the electricity power can be calculated based on Eq. (10).

2.3 Governing Equations for Modelling the Thermosyphon

The structure shown in Fig. 1 is simulated using CFD models as described here. To simulate the phase-change material we use the continuity equation using VOF model (Volume fraction equation).

Continuity equations:

$$\frac{\partial}{\partial t} (V_{f_l} \rho_l) + \nabla \cdot (V_{f_l} \rho_l \vec{v}_l) = -\dot{m}_{lg} \quad (11)$$

V_{f_l} is volume fraction of liquid phase, ρ_l is density of liquid phase. \dot{m}_{lg} is the mass transfer term defined from liquid phase to gas phase during phase change. Equation 11 is solved for liquid phase, then the secondary-phase (gas) volume fraction is:

$$V_{f_g} = 1 - V_{f_l} \quad (12)$$

Momentum equation:

$$\frac{\partial}{\partial t}(\rho \vec{v}) + \nabla \cdot (\rho \vec{v} \vec{v}) = -\nabla P + \nabla \cdot [\mu(\nabla \vec{v} + \nabla \vec{v}^T)] + \rho \vec{g} + \overrightarrow{F_{CSF}} \quad (13)$$

Here, the first term on the left hand side represents unsteady acceleration of momentum and the second term defines the momentum acceleration due to convection. On the right hand side, pressure gradient is defined by the first term and the second term accounts for the viscous force effects. The third term is gravitational force applied on the volume. Additional forces such as surface tension are taken into account using the last term.

$$F_{CSF} = 2\sigma \frac{V_{f_l} \rho_l \nabla V_{f_v} + V_{f_v} \rho_v \nabla V_{f_l}}{\rho_l + \rho_v}$$

$$\sigma = 0.09805856 - 1.845 \times 10^{-5}T - 2.3 \times 10^{-7}T^2 \quad (14)$$

Eq. (14) includes the surface tension along the liquid-gas interface [6]. This equation is solved throughout the domain, and the computed velocity field is shared among the phases.

Energy equation:

$$\frac{\partial}{\partial t}(\rho E) + \nabla \cdot (\vec{v}(\rho E + P)) = \nabla \cdot (k \nabla T) + S_e \quad (15)$$

In the energy equation, the first term is transient change of energy and the second term represents the rate of change of energy due to fluid motion. On the right side, the first term

serves as the divergence of heat flux. The last term is the source term from phase change effect in this simulation.

As we defined a mass transfer to simulate phase change, there will be accompanied energy source terms [26]:

$$S_e = \dot{m}_{lg} h_l \quad (16)$$

This source term is added to energy equation, it defines energy change accompanied with the defined mass transfer process. \dot{m}_{lg} is the mass transfer term defined in the continuity equation and h_l is the latent heat.

In the solid region, which includes the copper pipe and TE legs, the energy equation can be expressed as:

$$\frac{\partial}{\partial t}(\rho h) = \nabla \cdot (k \nabla T) \quad (17)$$

where ρ and k are density and thermal conductivity of the solid respectively, and h is sensible enthalpy.

2.4 Boundary Conditions & Initialization

Fig. 4b summarizes the boundary conditions used. Both top and bottom of the pipe are insulated. Water is used as the working fluid. The filling ratio (liquid volume occupancy percentage) of the thermosyphon is set to 0.4. The incoming heat flux is set as 738 W/m², which is calculated from Eq. (1). Radiation heat loss is governed by Eq. (5) on the evaporator. And the radiation heat transfer coefficient is set as 0.75 W/m²K for most cases. For a few

points, UDF is used to simulate the radiation heat loss. A forced convection value was chosen as $1000 \text{ W/m}^2\text{K}$, determined from Eq.(18) and defined on the condenser [27].

$$Nu_{cyl} = \frac{hD}{k} = 0.3 + \frac{0.62Re^{1/2}Pr^{1/3}}{[1+(0.4/Pr)^{2/3}]^{1/4}} \left[1 + \left(\frac{Re}{282000}\right)^{5/8}\right]^{4/5} \quad (18)$$

During solution initialization, the temperature of all zones are set as 360 K. And the water filling area ($x = 0:0.2$ and $y = 0:0.0034$) is marked and patched to hold the temperature at 373 K and liquid ratio at 1. In this way, we ‘filled’ the pipe with liquid water. To reduce the computational cost, we chose the initial temperature of all zone to be 360 K and the liquid temperature to be 373 K.

SIMPLE algorithm for pressure-velocity coupling and second-order upwind scheme for momentum and energy are used. QUICK and PRESTO for volume fraction and pressure are carried out. Transient calculations with a time step of 0.01 s are performed. After 100-200 s, both the variations of the evaporator temperature and the condenser temperature are relatively small over a large time range. And the results at 200 s are extracted for further analysis.

Chapter 3 Experiments

3.1 Experimental Design

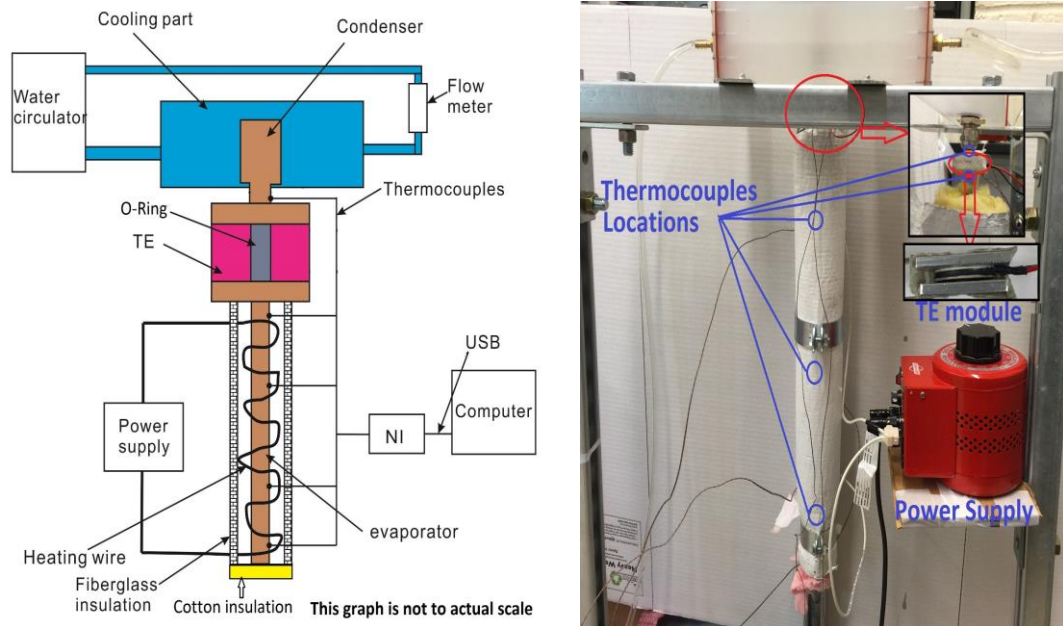


Fig. 5. Experimental setup.

(a), Schematic drawing of experimental setup; (b) Picture of the home-made setup.

To further validate the simulation and examine the feasibility of this parallel design, an experimental setup was built and tested. Fig. 5 (a) shows the illustrative design of the setup. Fig. 5 (b) displays the actual device. Six type-K thermocouples were used to measure the temperature across the thermosyphon. One heat cable was uniformly twisted around the thermosyphon to provide constant heat flux into this system. Using a Slide Regulator variable voltage power supply a voltage of 53.8 V was measured across the terminal output. Together

with the resistance of the cable, the heating power into the system was determined. The cooling rate (h) was determined by solving for Reynolds number around a cylinder in flow (condenser bulb). The Reynolds number was determined to be 47.42. Using Nusselt, Prandtl numbers and Eq. (18), the convection coefficient of the cooling water was determined to be $238.43 \text{ W/m}^2\text{k}$. Fiberglass insulation was applied to prevent heat leakage along the setup. The convective heat loss value $1.56 \text{ W/m}^2\text{k}$ was estimated from the fiberglass thickness and its material properties. Water flowed past the condenser in a three-walled, rectangular, top-open chamber and served as the cooling source.

3.2 System Description

3.2.1 TE Module

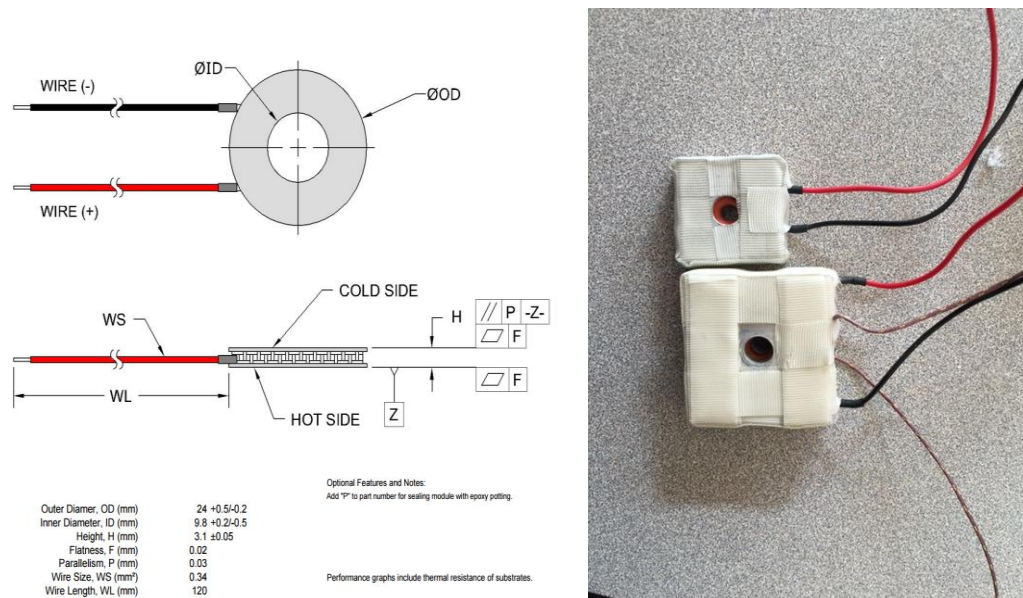


Fig. 6. (a) Specifications for CJ-38-1.0-0.8, (b) Actual wrapped TE module.

Because heat pipe is going through the TE module, a commercial TE module manufactured by TE Technology, Inc. is used. This Center Hole TE module is plotted to prevent steam

damage from possible leakages from the O-ring sealing. The dimension details for this TE module is shown in Fig. 6 (a). In the actual experiments, two aluminium plates are used to enhance the conduction heat transfer and also serve as supports for the module as shown in Fig. 6 (b).

3.2.2 Heater



Fig. 7. Wrapping of the wire heater.

A High-Temperature Heat Cable with cord and plug is used to heat up the device. This cable is purchased from McMaster Carr. Based on the resistance of the heater, a voltage about 53.8 V is sent by the power supply to simulate the heating input.

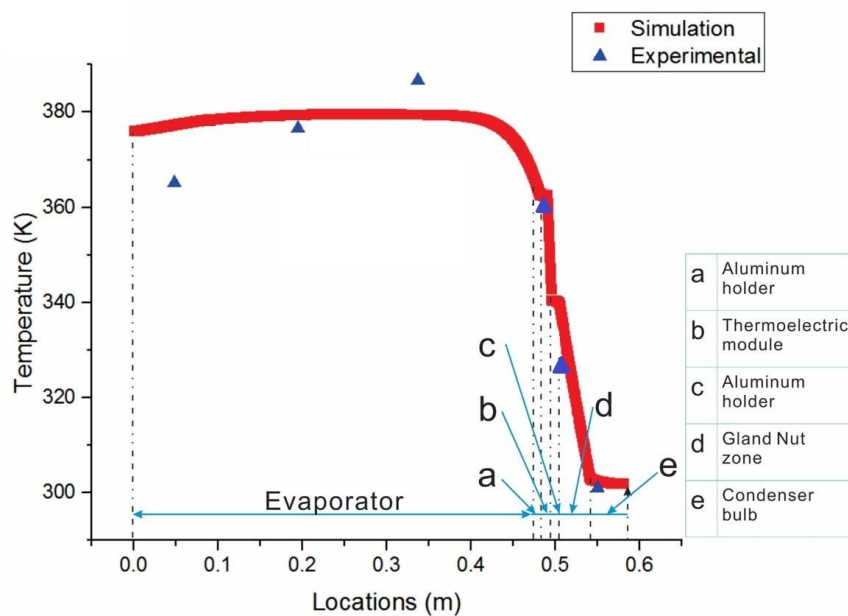


Fig. 8. A failure experimental result due to nonuniform heating.

Fig. 8 shows a bad temperature compare from previous experiment. We could see that the temperature matching in the evaporator zone is not as good as expected. This is due to nonuniform wrapping of the wire heater around the heat pipe. From this result, it can be seen that heat pipe is sensitive the heating inputs. This problem could be solved by uniformly distributing the wire heater along the evaporator. And a much better matching is obtained in Fig. 11.

3.2.3 Heat Pipe

A 2 m long full heat pipe is cut into two pieces: Evaporator and Condenser. A rubber O-Ring is used to connect these two pieces and to prevent steam leakages. The leakage could be well controlled with this O-Ring. When steam leakage happens (unusual, but happens once), there will be less or even no water inside the heat pipe. The heat pipe is no longer behaving like a 'heat pipe' (in other words, there is no phase change heat transfer inside the device), which results in a much higher evaporator temperature.

3.2.4 Water Cooling Channel

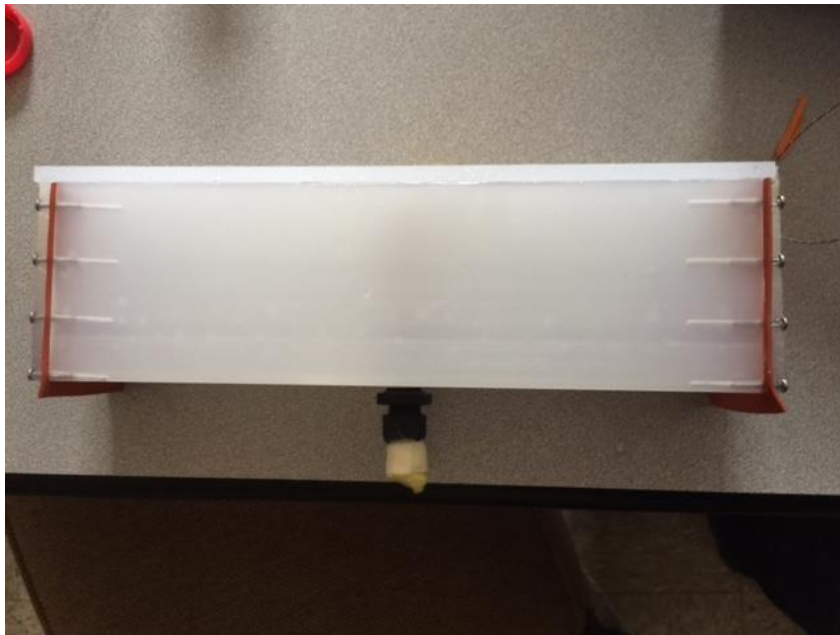


Fig. 9. Water cooling channel fabricated (in actual experiments, the black gland nut is replaced by a silver metallic gland nut).

A U-Channel shaped chemical-resistant polypropylene block is used as the main body of the water cooling channel. And two square polypropylene pieces and two rubber gaskets are fabricated to prevent leaking from the two ends of the channel. The connections are achieved mostly with screws. Super glue could be used to block overflow from the top end.

3.2.5 Thermocouples

6 glass braided insulated 36 gauge K-type thermocouples together with a 4-channel National Instrument thermocouple data acquisition module NI-9211 are used to measure the temperature on the surface of the heat pipe. The 6 thermocouples are attached to the surface by thermal paste and strengthened by insulating tapes. In the initial phase, 4 thermocouples are connected to the computer. After about 30 mins, temperatures did not change. And we

replaced two out of four already-measured thermocouples by two unmeasured thermocouples. In this way, temperatures at 6 locations are measured.

3.2.6 System Insulation

For a water-heating system, thermal insulation is crucial to its performance. A rigid high-temperature fiberglass pipe insulation is used to wrap most of the heat pipe. And cotton insulation is applied to the uncovered points, especially the bottom of the heat pipe and the connection between evaporator and condenser.

3.2.7 Accessories

The system is supported by steel-made strut channels. A slide regulator variable voltage power supply provides AC heating power to the heater. An aquarium water pump is used for pumping the water flow across the condenser. And the flow rate is too low to be measured by the rotor flow meter, so we estimated the volume flow rate by measuring the continuous flow with a 500 ml bottle and a timer.

Chapter 4 Results & Discussion

4.1 Comparison of Experiments and Simulation

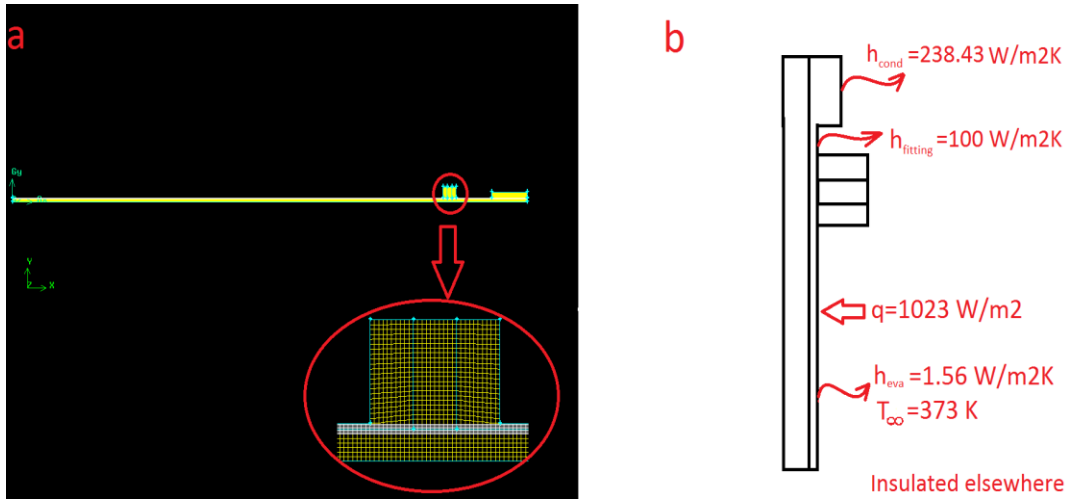


Fig. 10. (a) Experimental meshes used, (b) Boundary conditions used for modeling the experimental results.

A mesh to model the experiment was created with identical features to the existing prototype. The experimentally predetermined uniform heat flux (1023 W/m^2), convective heat loss ($1.56 \text{ W/m}^2\text{K}$) and cooling rate ($238.43 \text{ W/m}^2\text{K}$) were applied to the evaporator and condenser respectively. One fitted cooling rate ($100 \text{ W/m}^2\text{K}$) was set for the area covered by the gland nut. The rest of the system was set as insulated like the experiment.

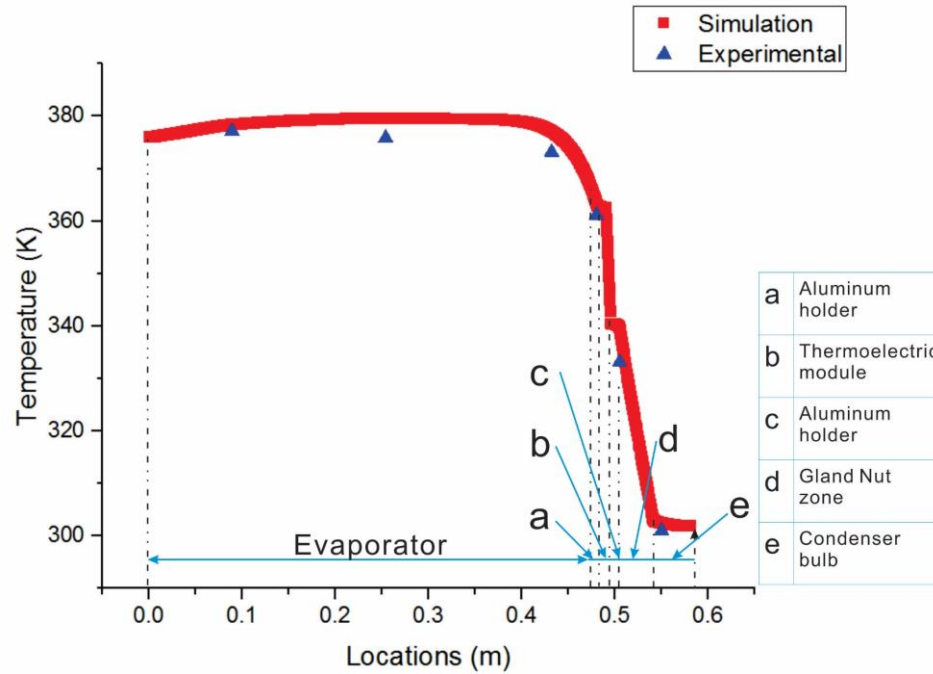


Fig. 11. Comparison of Experimental Values and Simulation Results for prototype.

In Fig. 11, the red line represents the simulation results and the blue upper triangles are the experimental data. From Fig. 11, very good agreements can be observed between simulation and experimental data.

One obvious shortcoming of this setup is the high temperature on the condenser part. This reduces the efficiency and performance of the TE module. One possible method to improve the setup is: fabricate a separate piece that ensures that both the gland nut zone and even the top surface of the aluminium could be cooled by flowing water.

4.2 Parallel System Optimization

In a solar energy collecting system, the dimensions of the collector have a crucial impact on its performance. In the parallel design, TEs are used to generate electricity. The geometry of

the TEs also affects the system performance. In this section, we study the effect of the geometrical parameters on the hybrid device efficiency to provide guidance for practical applications. In optimization, the parameters are set as described in Fig. 4 (b) except for the studied parameter. And most of the results shown below are computed without UDF except for the red circle and square points.

4.2.1 Effect of Thickness of TE

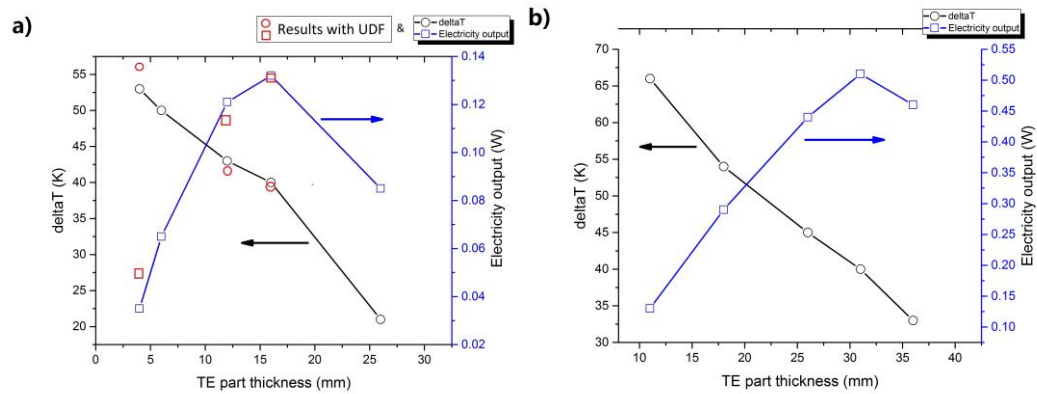


Fig. 12. Effect of thickness of TE on the performance of the thermoelectric modules in parallel design. Optimization of the output electric power for pipe radius of (a) $r = 4$ mm, and (b) $r = 11$ mm.

In Fig. 12 (a), the red circles and the red squares represent the results with the implementation of UDF. While the rest results are calculated without UDF. For a given pipe radius and TE part length, there is always a corresponding optimized TE thickness. The proper geometry is explained with Eq. (10). As the TE part thickness is increased, heat transfer rate through TE increases, but the temperature difference across the TE and the efficiency of the TE decreases. A balance between these two effects results in an optimized TE part thickness. As the TE thickness (t_{TE}) increases, thermal resistance of the TE decreases, resulting in a lower

temperature difference (ΔT) as shown in Fig. 12. A larger t_{TE} will result in more heat transport and higher electrical outputs. Therefore, optimized power output can be calculated by balancing these two effects. For a pipe radius of $r = 4$ mm, the maximum power output is 0.13 W, while a bigger pipe with a radius of 11 mm which has a higher heat input, will produce 0.5 W power.

4.2.2 Effect of Length of TE

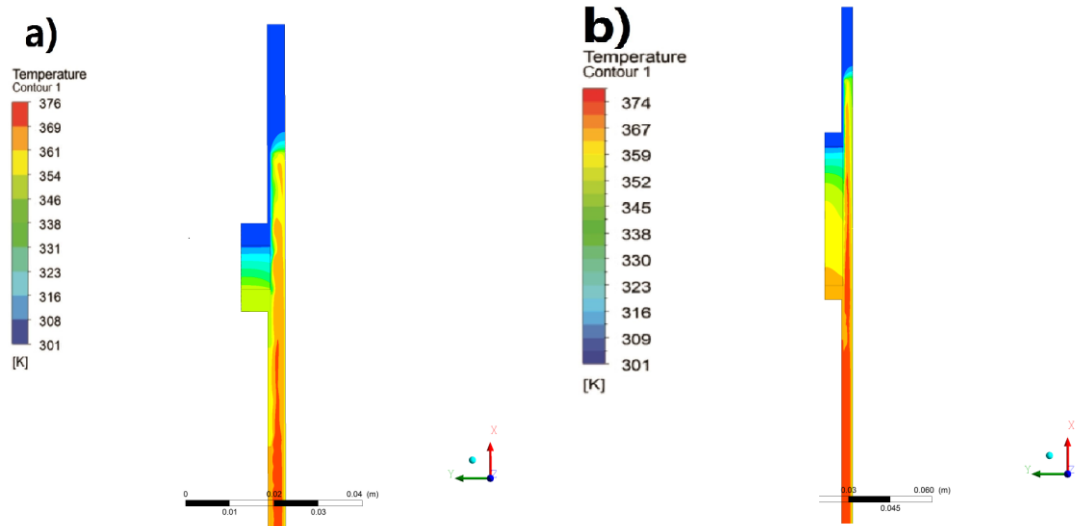


Fig. 13. Temperature plot in cylindrical coordinates for different TE part length.

(a): $L = 1$ cm;(b): $L = 5$ cm.

Figure 13 shows the temperature contours of condenser, TE and part of the evaporator. The water cooling flux applied on the condenser (with $h=1000 \text{ Wm}^{-2}\text{K}^{-1}$) keeps it at a low temperature. The solar radiation heat is trapped by the heat pipe by using the selective surface and the glass layer and results in a relatively high temperature for the evaporator. Due to the thermal conductivity difference of copper and BiSbTe, most of the temperature drop is

observed over the TE legs. From Fig. 13, we can see that a longer TE part length results in a larger temperature difference and therefore higher TE efficiency. However, shorter TE legs have larger temperature gradients, which result in larger heat transfer fluxes and larger power outputs. Since TE power output is a mixed result of efficiency and heat transfer rate through it, evaluation of Eq. (10) is necessary.

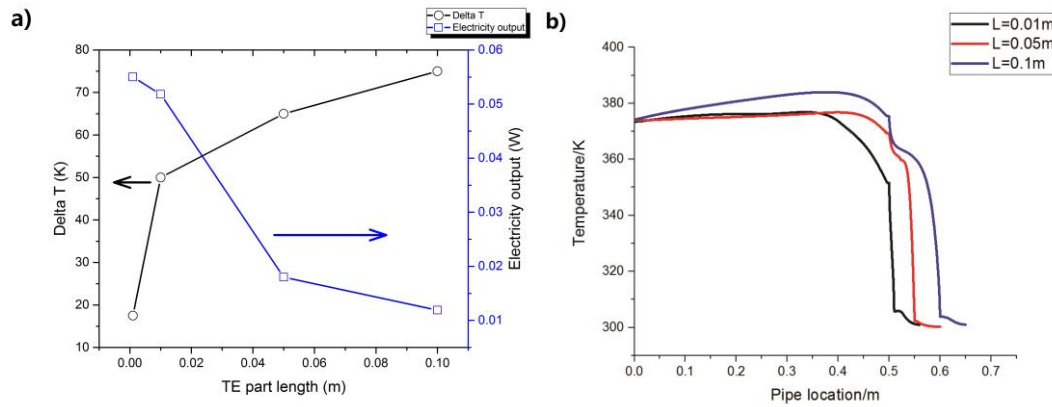


Fig. 14. (a) Effect of length of TE, (b) Temperature plot with different TE part length.

Figure 14 shows temperature profile along the heat pipe for different TE lengths. We see that the temperature difference increases as we increase TE part length, but the electricity produced is decreasing as a result of reduction in temperature gradient. Since TE power output is a combined result of above two factors, from Eq. (10), the TE part length should be chosen in order to hold the balance between TE efficiency and electricity output. For our further analysis, we choose this length to be 0.01 m.

4.2.3 Effect of Pipe Radius

Due to the fact that the solar energy collected by a 4mm radius pipe is as small as 10 W (for a 0.5 length pipe) and considering the efficiency of TEs, a small power can be expected.

Increasing the pipe radius will evidently boost the collected solar energy, thus raise the TE power output.

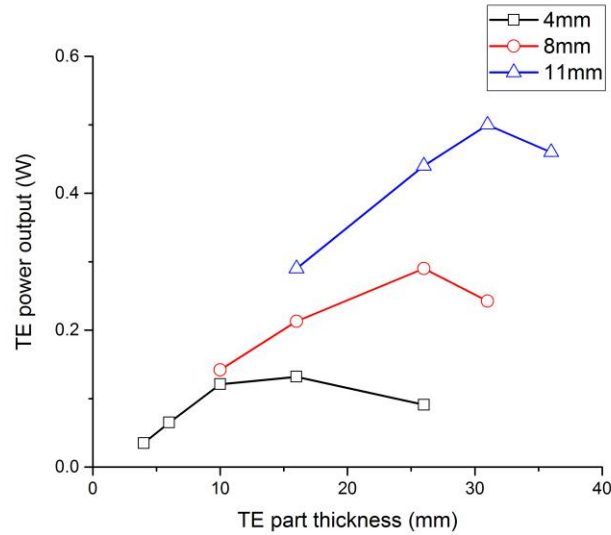


Fig. 15. Thermoelectric power output versus TE part thickness.

It can be seen from Fig. 15 that a higher power output is indeed seen when increasing heat pipe radius. The logic behind this is that a bigger pipe radius engenders a larger solar collector area, which allows more solar energy to come in. A power of 0.5 W has been shown when we have a pipe with radius of 11 mm. In terms of land usage, the area occupied by such pipe on the roof is about 0.0308 m^2 , which means an electrical power density of 16 W/m^2 could be harvested in addition to the thermal power density of about 780 W/m^2 .

Chapter 5 Conclusion

In this paper, comprehensive numerical simulation and experimental tests are carried out to investigate the feasibility and performance of thermoelectric modules added thermally in parallel to a two-phase thermosyphon. Thermoelectric modules were added as topping cycles to cogenerate electric power. We demonstrated that even without solar concentration, electrical powers as high as 0.5 W are possible. The land usage required is minimal and thus the power density is equivalent to 16 W/m^2 . The electrical power obtained is an order of magnitude lower than typical electrical powers obtained by using solar cells (in the case of commercial solar cells typical peak powers are 150 W/m^2). However, a much smaller fraction of the area is used by the thermoelectric materials, and the hybrid power generated is more than 780 W/m^2 . The electrical power could be increased by further optimization of the pipe and thermoelectric dimensions. In addition, one can increase the boiling point of the phase-change material or the solar incoming flux to potentially increase the temperature difference and therefore increase the output electrical power of the thermoelectric modules to make it more practical for residential applications.

Experimental realization of this system is performed and the measured results are compared with the simulation results. There exists a very good match between the simulation and experiments. The experimental results tested the feasibility of this design. It validated the simulation results and provide directions for further simulations.

In the future industrialization process, multiple heat pipes could be connected in series and provide a reasonable amount of both thermal and electrical power to household applications.

References

- [1] M. Thirugnanasambandam, S. Iniyan, R. Goic, A review of solar thermal technologies, *Renewable and sustainable energy reviews*, 14 (2010) 312-322.
- [2] X. Zhou, F. Wang, R.M. Ochieng, A review of solar chimney power technology, *Renewable and Sustainable Energy Reviews*, 14 (2010) 2315-2338.
- [3] IRENA, Solar Heating and Cooling for Residential Applications, IEA-ETSAP and IRENA Technology Brief, E21 (2015).
- [4] A. Faghri, Heat pipe science and technology, Global Digital Press, 1995.
- [5] A. Alizadehdakhl, M. Rahimi, A.A. Alsairafi, CFD modeling of flow and heat transfer in a thermosyphon, *International Communications in Heat and Mass Transfer*, 37 (2010) 312-318.
- [6] B. Fadhl, L.C. Wrobel, H. Jouhara, Numerical modelling of the temperature distribution in a two-phase closed thermosyphon, *Applied Thermal Engineering*, 60 (2013) 122-131.
- [7] T. Bergene, O.M. Løvvik, Model calculations on a flat-plate solar heat collector with integrated solar cells, *Solar energy*, 55 (1995) 453-462.
- [8] N. Miljkovic, E.N. Wang, Modeling and optimization of hybrid solar thermoelectric systems with thermosyphons, *Solar Energy*, 85 (2011) 2843-2855.
- [9] T.T. Chow, A review on photovoltaic/thermal hybrid solar technology, *Applied Energy*, 87 (2010) 365-379.
- [10] W. He, Y. Su, Y.Q. Wang, S.B. Riffat, J. Ji, A study on incorporation of thermoelectric modules with evacuated-tube heat-pipe solar collectors, *Renewable Energy*, 37 (2012) 142-149.
- [11] D. Kraemer, B. Poudel, H.P. Feng, J.C. Caylor, B. Yu, X. Yan, Y. Ma, X. Wang, D. Wang, A. Muto, K. McEnaney, M. Chiesa, Z. Ren, G. Chen, High-performance flat-panel solar thermoelectric generators with high thermal concentration, *Nature materials*, 10 (2011) 532-538.
- [12] W. He, Y. Su, S.B. Riffat, J. Hou, J. Ji, Parametrical analysis of the design and performance of a solar heat pipe thermoelectric generator unit, *Applied Energy*, 88 (2011) 5083-5089.
- [13] M. Zebarjadi, Electronic cooling using thermoelectric devices, *Applied Physics Letters*, 106 (2015) 203506.
- [14] Ansys, Ansys Fluent Theory Guide, Ansys Fluent Theory Guide, (2009).
- [15] G. de Vahl Davis, Natural convection of air in a square cavity: a bench mark numerical solution, *International Journal for numerical methods in fluids*, 3 (1983) 249-264.
- [16] Y. Zhang, A. Faghri, M.B. Shafii, Capillary Blocking in Forced Convective Condensation in Horizontal Miniature Channels, *Journal of Heat Transfer*, 123 (2001) 501.
- [17] K. Kafeel, A. Turan, Simulation of the response of a thermosyphon under pulsed heat input conditions, *International Journal of Thermal Sciences*, 80 (2014) 33-40.
- [18] K. Emer, Reference Solar Spectral Irradiance: Air Mass 1.5, <http://rredc.nrel.gov/solar/spectra/am1.5/>, American Society for Testing and Materials (ASTM) Terrestrial Reference Spectra for Photovoltaic Performance Evaluation, (<http://rredc.nrel.gov/solar/spectra/am1.5/>).

- [19] Y.A. Cengel, A.J. Ghajar, H. Ma, Heat and Mass Transfer: Fundamentals & Applications, 4e, McGraw-Hill, 2011.
- [20] AlanodSolar, Alanod-Solar® Image-Broschüre, © ALANOD GmbH & Co. KG, (<http://www.alanod.com/en>).
- [21] Y. Jaluria, Computational heat transfer, CRC Press, 2002.
- [22] Fluent, Fluent UDF Manual, Fluent UDF Manual, (2006).
- [23] B. Poudel, Q. Hao, Y. Ma, Y. Lan, A. Minnich, B. Yu, X. Yan, D. Wang, A. Muto, D. Vashaee, High-thermoelectric performance of nanostructured bismuth antimony telluride bulk alloys, Science, 320 (2008) 634-638.
- [24] X. Yan, B. Poudel, Y. Ma, W.S. Liu, G. Joshi, H. Wang, Y. Lan, D. Wang, G. Chen, Z.F. Ren, Experimental Studies on Anisotropic Thermoelectric Properties and Structures of n-Type Bi₂Te_{2.7}Se_{0.3}, Nano letters, 10 (2010) 3373-3378.
- [25] G.S. Nolas, J. Sharp, J. Goldsmid, Thermoelectrics: basic principles and new materials developments, Springer Science & Business Media, 2013.
- [26] S.C.K. De Schepper, G.J. Heynderickx, G.B. Marin, Modeling the evaporation of a hydrocarbon feedstock in the convection section of a steam cracker, Computers & Chemical Engineering, 33 (2009) 122-132.
- [27] S. Churchill, M. Bernstein, A correlating equation for forced convection from gases and liquids to a circular cylinder in crossflow, ASME, Transactions, Series C-Journal of Heat Transfer, 99 (1977) 300-306.